Nanoscale

ROYAL SOCIETY OF CHEMISTRY

PAPER

View Article Online
View Journal | View Issue

Cite this: *Nanoscale*, 2024, **16**, 11096

Lattice capacity-dependent activity for CO_2 methanation: crafting Ni/CeO_2 catalysts with outstanding performance at low temperatures†

Kun Liu,*[b] Yixin Liao,[a] Peng Wang,[c] Xiuzhong Fang,[a] Jia Zhu,[d] Guangfu Liao *[e] and Xianglan Xu *[a]

In the pursuit of understanding lattice capacity threshold effects of oxide solid solutions for their supported Ni catalysts, a series of Ca^{2+}-doped CeO_2 solid solutions with 10 wt% Ni loading (named Ni/$Ca_xCe_{1-x}O_y$) was prepared using a sol–gel method and used for CO_2 methanation. The lattice capacity of Ca^{2+} in the lattice of CeO_2 was firstly determined by the XRD extrapolation method, corresponding to a Ca/(Ca + Ce) molar ratio of 11%. When the amount of Ca^{2+} in the $Ca_xCe_{1-x}O_y$ supports was close to the CeO_2 lattice capacity for Ca^{2+} incorporation, the obtained Ni/$Ca_{0.1}Ce_{0.9}O_y$ catalyst possessed the optimal intrinsic activity for CO_2 methanation. XPS, Raman spectroscopy, EPR and CO_2-TPD analyses revealed the largest amount of highly active moderate-strength alkaline centers generated by oxygen vacancies. The catalytic reaction mechanisms were revealed using *in situ* IR analysis. The results clearly demonstrated that the structure and reactivity of the Ni/$Ca_xCe_{1-x}O_y$ catalyst exhibited the lattice capacity threshold effect. The findings offer a new venue for developing highly efficient oxide-supported Ni catalysts for low-temperature CO_2 methanation reaction and enabling efficient catalyst screening.

Received 31st March 2024,
Accepted 7th May 2024

DOI: 10.1039/d4nr01409j

rsc.li/nanoscale

1. Introduction

With the significant consumption of carbon-based energy sources, the amount of CO_2 emitted into the atmosphere is continually increasing and has caused great damage to the environment.[1–4] Currently, to achieve the goal of carbon neutrality, the relevant research around the capture, conversion and utilization of CO_2 has received extensive attention.[5–7] In this context, CO_2 methanation reaction has attracted much attention due to its potential to enable the reaction of industrial waste CO_2 with sustainable hydrogen gas to obtain high value-added methane and alleviate environmental problems.[8–12] CO_2 methanation reaction is an extremely exothermic reaction, presenting significant kinetic challenges.[8] Thus, there is a strong desire to develop cost-effective catalysts capable of achieving high activity at low temperatures for practical applications (Fig. 1a). Compared to extensively studied supported precious metals, Ni-based catalysts offer several distinct advantages including a readily available source, cost-effectiveness, and high performance.[13–18] Thus, oxide-supported Ni-based catalysts have garnered significant attention for CO_2 methanation.[11,16–18]

Among the various Ni-based catalysts,[19–25] CeO_2 support has been widely employed due to its abundant oxygen vacancies and robust oxygen storage capacity,[18,26–30] which holds the potential to enhance the low-temperature reaction activity.[11,18,21,29] In the pursuit of preparing high and low temperature-active catalysts, strategies such as hydrogen-rich stream,[23] modifying with Ce,[24] and constructing interfaces[25] have shown promising results.

In addition, oxide solid solutions offer a promising avenue for enhancing the low-temperature activity.[11,31] It has been reported that metal oxide solid solutions exhibit distinct properties. When compared to their individual components, they typically demonstrate improved and stimulating physicochemical characteristics, thereby exerting a positive impact on the catalytic performance in various reactions.[32–36] The creation of a solid solution structure can lead to substantial enhancements in the thermal endurance, porous structure and abundance of surface-active oxygen sites. These improve-

[a]*Key Laboratory of Jiangxi Province for Environment and Energy Catalysis, Institute of Rare Earths, School of Chemistry and Chemical Engineering, Nanchang University, Nanchang, Jiangxi 330031, China. E-mail: xuxianglan@ncu.edu.cn*
[b]*School of Resources and Environment, Nanchang University, 999 Xuefu Road, Nanchang, Jiangxi, 330031, China. E-mail: liukun@ncu.edu.cn*
[c]*Shandong Chambroad Petrochemicals Co., Ltd, Binzhou, Shandong 256500, China*
[d]*College of Chemistry and Chemical Engineering, Jiangxi Normal University, Nanchang, Jiangxi 330022, China*
[e]*College of Materials Engineering, Fujian Agriculture and Forestry University, Fuzhou 350002, China. E-mail: liaogf@mail2.sysu.edu.cn*
† Electronic supplementary information (ESI) available. See DOI: https://doi.org/10.1039/d4nr01409j

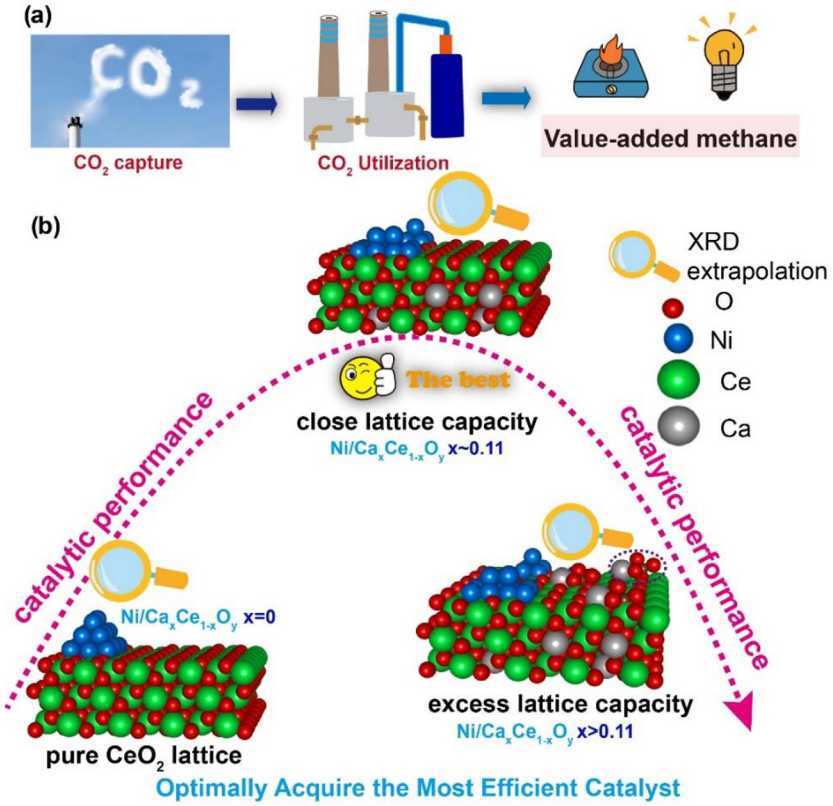

Fig. 1 Overview of this study. (a) Hydrogenating industrial CO_2 emissions with renewable hydrogen to produce high-value methane to achieve carbon neutrality. (b) In a groundbreaking approach, the lattice capacity of Ca^{2+} in CeO_2 was precisely quantified utilizing the XRD extrapolation method.

ments are usually attributed to lattice distortion and the generation of lattice defects, both of which typically contribute to enhanced catalytic performance.[37–39] In our previous work, Ce–M–O solid solutions were investigated, where M represents cations such as Mg, Ca, Sr, and Ba.[11] The creation of stable solid solution arrangement structures for M, such as Mg^{2+} and Ca^{2+}, boasts a notably higher amount of surface oxygen vacancies and more moderate alkaline sites when compared to pure CeO_2, which not only substantially augments the oxygen storage capacity but also significantly boosts the turnover frequency and enhances the low-temperature reaction activity for CO_2 methanation. Conversely, the alkaline earth metals Sr and Ba, with their large ionic radii, cannot fit into the ceria lattice to form solid solutions, which leads to fewer active oxygen vacancies. Instead, they predominantly accumulated on the support surface as highly alkaline oxides and carbonates. This excessive CO_2 adsorption capacity resulted in poor catalytic performance.[40] Solid solution catalysts have been extensively investigated and have frequently exhibited enhanced activity and stability when compared to individual metal oxides.[10,26,34,37,38]

In our previous publications, we devised an XRD extrapolation technique to quantify the lattice capacity of a solute cation within the lattice of a solvent metal oxide in oxide solid solutions[39,40] and discovered that pure oxide solid solutions act as catalysts with a lattice capacity threshold effect on reactions.[10,26,36,37] This study marks a significant departure from our prior research on solid solution catalysts as it is based on our preliminary discovery that many metal oxide solid solutions can themselves act as catalysts, exhibiting a lattice capacity threshold effect in specific reactions. In this work, we delve into the lattice capacity threshold effect in supported catalysts, with a particular focus on Ni catalysts supported on Ca^{2+}-doped CeO_2 solid solutions (Fig. 1b). A series of $Ca_xCe_{1-x}O_y$ supports with diverse contents of calcium oxide was prepared by a sol–gel method (x = 0.05–0.55), and the supported Ni materials were obtained by an incipient impregnation method with 10 wt% Ni loading. The XRD extrapolation method was adopted to measure the lattice capacity; the activity of the $Ca_xCe_{1-x}O_y$-supported Ni catalysts exhibited the lattice capacity threshold effect for CO_2 methanation. The nature of the threshold effect was revealed by various characterization methods, such as XRD, H_2-TPR, Raman, XPS, and CO_2-TPD.

2. Experimental

2.1 Catalyst preparation

A series of Ca^{2+}-doped CeO_2 supports with varying amounts of Ca cations was synthesized using a sol–gel method. Initially, $Ce(NO_3)_3{\cdot}6H_2O$ (Shanghai Macklin, A.R) and $Ca(NO_3)_2{\cdot}4H_2O$

(A.R.) were dissolved in 50 mL solution, with different Ca/Ce molar ratios named *x*. Subsequently, citric acid (Shanghai Macklin, A.R.), equivalent to 0.6 times the molar ratio of $Ce(NO_3)_3{\cdot}6H_2O$ and $Ca(NO_3)_2{\cdot}4H_2O$, was added. Next, the citric acid was burned off at 220 °C. Subsequently, the material was calcined at a heating rate of 2 °C min^{-1}, reaching 700 °C, and was held at this temperature for 4 h to produce $Ca_xCe_{1-x}O_y$. It should be noted that the synthesis protocol for CeO_2 was identical to that of $Ca_xCe_{1-x}O_y$, with the sole distinction being the absence of Ca metal.

The 10 wt% $NiO/Ca_xCe_{1-x}O_y$ materials were synthesized using an impregnation method. Typically, a specific quantity of $Ca_xCe_{1-x}O_y$ (*vide supra*) was dropped into $Ni(NO_3)_2{\cdot}6H_2O$ solution and stirred for 2 h. Subsequently, it was dried at 110 °C. Finally, the material was calcined at 450 °C to obtain $NiO/Ca_xCe_{1-x}O_y$. The final catalysts were defined as $Ni/Ca_xCe_{1-x}O_y$. The samples underwent reduction with a 10% H_2/Ar gas mixture, maintained under 450 °C. The chemical compositions of the samples were validated *via* ICP-AES analysis.

2.2 Activity evaluation

CO_2 methanation evaluation using 10 wt% $Ni/Ca_xCe_{1-x}O_y$ catalysts was carried out in the following manner. Initially, the catalyst powder was mixed with an appropriate amount of quartz sand and subjected to compression molding (catalyst : quartz sand = 1 : 1). 100 mg of fresh catalyst underwent *in situ* reduction at 450 °C for 2 h with a gas mixture comprising 10% H_2 and 90% Ar. Subsequently, the temperature was reduced to room temperature, followed by the introduction of high-purity H_2 (99.99%) and high-purity CO_2 (99.99%) (H_2/CO_2 = 4). CO_2 and H_2 reactants were mixed in 1 : 4 stoichiometric ratio, resulting in a WHSV of 36 000 mL per h per gram of the catalyst. The outlet gas was condensed, then analyzed online using a GC9310 gas chromatograph. High-purity argon gas (99.99%) was employed as the carrier gas in chromatography. A TDX-01 molecular sieve column with an inner diameter of 2 mm and a length of 3 m was utilized for the separation of H_2, CO, CH_4, and CO_2. The tail gas was subsequently passed through a gas chromatograph equipped with a TDX-01 column, and carbon conservation was applied using the peak area normalization method to calculate the conversion rate of the reaction. The detection of the separated substances (reactants and products) post-column separation was conducted using a thermal conductivity detector (TCD) in the GC9310 chromatograph. Before the test, steady-state kinetic data measurements were conducted. The CO_2 conversion (X_{CO_2}), CH_4 selectivity (S_{CH_4}) and CH_4 yield (Y_{CH_4}) were calculated as follows.

$$X(CO_2) = \frac{n(CH_4)_{out} + n(CO)_{out}}{n(CH_4)_{out} + n(CO_2)_{out} + n(CO)_{out}} \times 100\%$$

$$S(CH_4) = \frac{n(CH_4)_{out}}{n(CH_4)_{out} + n(CO)_{out}} \times 100\%$$

$$Y(CH_4) = X(CO_2) \times S(CH_4)$$

where $n(CO_2)$, $n(CH_4)$, and $n(CO)$ represent the respective molar amounts of each gas.

2.3 Catalyst characterization

The XRD patterns of the samples were acquired using a Bruker AXS D8Focus X-ray diffractometer instrument with Cu Kα radiation (operating at 40 kV and 30 mA). Scans spanned from 20° to 90° (2θ) at a 2° per minute ramp rate. Mean crystallite sizes were calculated using the Scherrer equation ($d = K\lambda/(B1/2\cos\theta)$, K = 0.89, λ = 1.5406 Å). The Raman spectra were obtained with an argon laser excitation source at 532 nm. CO_2-TPD was performed using a Micromeritics Auto Chem 2920 apparatus. High-purity helium was employed as the carrier and pretreatment gas, while high-purity CO_2 served as the adsorption gas. The reduced $Ni/Ca_xCe_{1-x}O_y$ catalysts were preheated to 400 °C, then cooled to room temperature, and purged with ultrahigh purity He for 0.5 h. Afterwards, the instrument program was ramped up to 700 °C. XPS was performed at room temperature under ultra-high vacuum conditions (300 W and 15 kV). EPR test was done at 77 K using a JEOL FA-200 EPR with 100 kHz field modulation and microwave frequency of 9067.558 MHz. H_2 temperature-programmed desorption (H_2-TPD) was conducted using a Micromeritics Auto Chem 2920 apparatus. Initially, 50 mg of the sample underwent heating at 400 °C for 30 min to eliminate any potential impurities. Subsequently, the sample was cooled to 50 °C and exposed to a flow of H_2 at 30 mL min^{-1} for 1 h to saturate the surface. This was followed by purging with ultrahigh purity Ar at the same flow rate for 30 min to remove any physically adsorbed H_2. Following these pretreatments, the catalyst was heated from 50 to 700 °C at a rate of 10 °C min^{-1}.

H_2-TPR experiments were conducted on a FINESORB 3010C instrument using 50 mg of the sample. Catalysts were pretreated in Ar flow at 120 °C for 30 min to remove impurities. Temperature was ramped from room temperature to 900 °C at 10 °C min^{-1} in a 10% H_2/Ar flow of 30 mL min^{-1}. H_2 consumption was monitored using a TCD with CuO (99.99%) as the calibration standard. Utilizing an *in situ* FTIR equipped with an MCT detector, capturing the intermediate species in the catalysts is a pivotal method for probing the reaction mechanisms. Before commencing experiments, the samples were pre-treated at 300 °C for 1 h in a high-purity Ar atmosphere. Subsequently, they were cooled to 50 °C, and the background spectra were obtained under Ar atmosphere. Following this, the gas was switched to a mixture of 4% H_2, 1% CO_2, and 95% Ar for CO_2 hydrogenation testing, with a controlled gas flow rate of 20 mL min^{-1}. The temperature was ramped from 50 °C to 400 °C to monitor the dynamic changes of the intermediate species within the samples. Infrared spectra were collected once all species reached a steady state at the set temperatures.

3. Results and discussion

3.1 Quantifying the lattice capacity of Ca^{2+} in CeO_2 through the XRD extrapolation method

XRD experiments were used to analyze $Ca_xCe_{1-x}O_y$ phases and Ca^{2+} lattice capacity in CeO_2. Fig. 2 and Fig. S1† display the

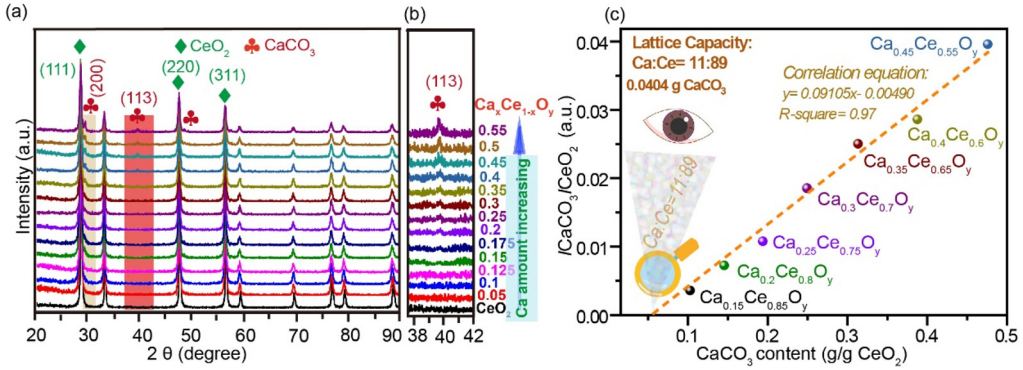

Fig. 2 (a and b) Complete and enlarged XRD patterns of the $Ca_xCe_{1-x}O_y$ support; (c) the lattice capacity quantification of CeO_2 for Ca^{2+} cations. The lattice capacity of Ca^{2+} in the lattice of the CeO_2 was firstly determined by the XRD extrapolation method, corresponding to a Ca/(Ca + Ce) molar ratio of 11% (see Fig. 2, S1† and Table 1).

results, and Table 1 summarized the phase compositions. For pure CeO_2, three prominent peaks at 2θ values of 28.90°, 47.77°, and 56.76° confirmed the cubic fluorite crystalline phase (Fig. 2).[11] The peaks at 31.13°, 42.91°, and 50.24° indicated the presence of $CaCO_3$. Low Ca content solid solution samples (*e.g.*, $Ca_{0.05}Ce_{0.95}O_y$ and $Ca_{0.1}Ce_{0.9}O_y$) showed only CeO_2 peaks, suggesting that Ca^{2+} incorporation into the CeO_2 lattice formed a solid solution. Increasing Ca content (x = 0.15 to 0.55) led to $CaCO_3$ phase emergence and weakened CeO_2 peaks (Fig. 2b), signaling excess Ca exceeding the lattice capacity and reacting with CO_2.[11] In Ce-rich Ce–Ca binary oxide supports with Ca/Ce < 15/85 (*e.g.*, $Ca_{0.05}Ce_{0.95}O_y$ and $Ca_{0.1}Ce_{0.9}O_y$), only broadened CeO_2 peaks were observed, indicating the Ca^{2+}-incorporated CeO_2 lattice. As Ca/Ce approached 15/85, subtle $CaCO_3$ peaks emerged at 42.91°. For clarity, Table 1 summarizes the phase compositions of supports with varying Ca/Ce ratios. The Ce^{4+} in CeO_2 possesses a coordination number (CN) of 8 and a radius measuring 0.97 Å. The radius of Ca^{2+} cations under a coordination number (CN) of 8 is 1.12 Å. In principle, the Ca^{2+} cations meet the required radius criteria for the formation of a solid solution structure.[41,42] Thus, there is high likelihood that Ca^{2+} cations were successfully integrated into the CeO_2 lattice matrix to form a solid solution. To prove this hypothesis, we meticulously determined and compared the 2θ and d-values associated with the most intense (111) peak of the CeO_2 phase as well as the mean crystallite sizes of CeO_2 (Fig. S1† and Table 1). Evidently, the 2θ and d values in all the Ca^{2+}-doped samples deviate from those of the parent CeO_2, confirming the successful incorporation of Ca^{2+} cations into the CeO_2 matrix, replacing a portion of the Ce^{4+} cations in the formed solid solution structure.

Our previous research has demonstrated that in the case of non-solid solutions, solute cations typically integrated into the matrix structure of a host metal oxide with a specific lattice capacity,[41,42] a quantifiable parameter that can be determined using the XRD extrapolation method developed by our team (Fig. 2c, fitting diagram). As outlined in our study, for some results of this partial substitution process, XRD analysis may not detect the presence of $CaCO_3$ phases due to their low concentration at this stage. Once the calcium content nears its saturation point within the lattice, the catalyst surface starts to facilitate the formation of polymeric and amorphous calcium carbonate species. Nevertheless, unless the $CaCO_3$ crystallites attained a specific crystalline dimension, typically about 5 nm, the $CaCO_3$ phase remains undetectable by XRD analysis.[11,41,42] Therefore, due to this limitation, for a more precise and dependable determination of the capacity threshold of calcium in the $Ca_xCe_{1-x}O_y$ solid solution, our research group has developed the XRD extrapolation method, which is widely recognized and employed.[11,41,42] The lattice capacity can only be extrapolated through the correlated line (Fig. 2c). Theoretically, the presence of crystalline $CaCO_3$ was intricately linked to the overall calcium content within the Ca–Ce binary oxide catalysts. The strength or prominence of its diffraction peaks serves as an indicator of the quantity of the $CaCO_3$ crystalline phase. The intensity of $CaCO_3$ at the (113) crystal plane that represents the peak of $CaCO_3$ was employed to quantify the extent of crystalline Ca^{2+} cations that entered the CeO_2 lattice matrix. In detail, the intensity (I_0) of the strongest peak of CeO_2 (111) was employed to normalize the I to get a series of I/I_0 ratios, which correlate to the quantity of $CaCO_3$ crystalline phase in the samples. I/I_0 ratios were plotted against the

Table 1 XRD results of $Ca_xCe_{1-x}O_y$ supports

Supports	CeO_2 (111) 2θ (°)	d^a (Å)	Phase composition	Crystalline size of CeO_2 (nm)
CeO_2	28.919	3.085	CeO_2	23.1
$Ca_{0.05}Ce_{0.95}O_y$	28.579	3.121	CeO_2 SS[b]	21.8
$Ca_{0.1}Ce_{0.9}O_y$	28.360	3.144	CeO_2 SS	18.2
$Ca_{0.125}Ce_{0.875}O_y$	28.400	3.140	CeO_2 SS + $CaCO_3$	19.0
$Ca_{0.25}Ce_{0.75}O_y$	28.420	3.138	CeO_2 SS + $CaCO_3$	19.8
$Ca_{0.4}Ce_{0.6}O_y$	28.421	3.136	CeO_2 SS + $CaCO_3$	20.7

[a] Calculated using Scherrer's equation for the diffraction pattern of (111) facets of CeO_2. [b] SS: solid solution.

$CaCO_3$ quantity, which was normalized by the CeO_2 content. A correlated line was obtained, which intersects the x axis at a point having an x-axis value of 0.0404 g $CaCO_3$ per gram CeO_2, which was equivalent to a Ca/Ce molar ratio of 11/89, corresponding to 11% of the Ce^{4+} cations that can be maximally substituted by Ca^{2+}, forming a stable solid solution (Fig. 2c). Once the Ca^{2+} content exceeds the lattice capacity, the surplus Ca^{2+} were could form free-state $CaCO_3$ species, aggregating and enriching on the surface. Typically, the $CaCO_3$ micro-crystallites can be clearly detected by XRD when their size reached or approached about 5 nm. Furthermore, their diffraction intensity increases with higher Ca content, as observed in the case of $Ca_xCe_{1-x}O_y$ (x = 0.15–0.55). Notably, for $Ca_{0.05}Ce_{0.95}O_y$ and $Ca_{0.1}Ce_{0.9}O_y$, since the Ca content remained within the lattice capacity of CeO_2 (Fig. 2a and b), all Ca^{2+} cations were incorporated into the lattice structure of CeO_2, thereby eluding detection through XRD analysis.[43,44]

3.2 The lattice capacity threshold effect of Ca^{2+} in CeO_2 on CO_2 methanation by Ni/$Ca_xCe_{1-x}O_y$ catalysts

To explore the lattice capacity threshold effect of these solid solutions, all the Ni/$Ca_xCe_{1-x}O_y$ catalysts were evaluated for CO_2 methanation (Fig. 3). For the parent Ni/CeO_2 catalyst, the overall activity increased as the temperature rose until reaching 350 °C, achieving a CO_2 conversion of 65% and CH_4 selectivity of 95%. Ni/$Ca_xCe_{1-x}O_y$ catalysts displayed the overall activity sequence of Ni/$Ca_{0.1}Ce_{0.9}O_y$ > Ni/$Ca_{0.05}Ce_{0.95}O_y$ > Ni/$Ca_{0.25}Ce_{0.75}O_y$ > Ni/$Ca_{0.4}Ce_{0.6}O_y$ > Ni/CeO_2; however, they have a similar CH_4 selectivity (Fig. 3). The Ni/$Ca_{0.1}Ce_{0.9}O_y$ catalyst exhibited the highest overall activity, achieving a remarkable 75% CO_2 conversion and complete CH_4 selectivity at 290 °C. The response data trends revealed that when the amount of Ca incorporated into the solid solution was below its lattice capacity, there was a gradual increase in CO_2 conversion. As the Ca content rose, the catalytic activity was further augmented. Conversely, when the Ca content surpassed the lattice capacity, the activity diminished with increasing Ca content. The optimal activity of the loaded Ni catalyst was achieved when the Ca doping content was aligned precisely with the lattice capacity threshold, enabling the creation of the highest possible quantity of a pure-phase solid solution on the carrier material (*i.e.*, 10 wt% Ni/$Ca_xCe_{1-x}O_y$). This indicated the presence of a lattice capacity threshold effect for dopant elements in oxide solid solution catalysts supporting Ni, highlighting its pivotal role in catalyst performance.

For better understanding the modification effects of varying calcium oxide content on the intrinsic activity, Arrhenius plots (Fig. 3c) were generated for all the catalysts. These plots were constructed using CO_2 conversion data below 10% to eliminate potential influences from mass and heat transfer effects. To provide a clearer understanding, we calculated R_w (mass normalized rate) and R_s (surface area normalized rate), representing CO_2 conversion rates at 250 °C, which are normalized by catalyst weights and surface areas and deter-

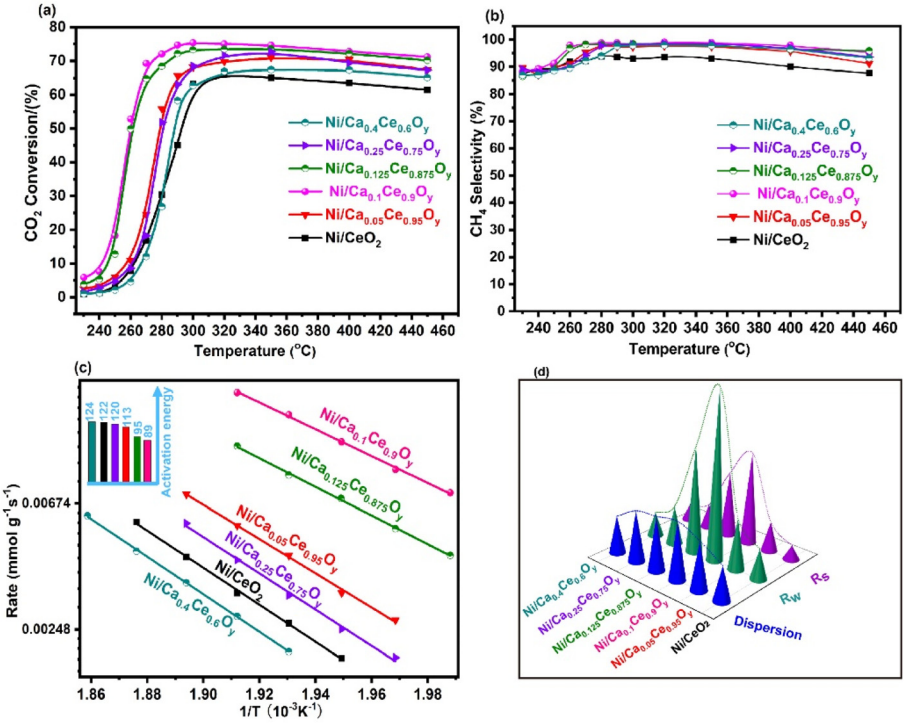

Fig. 3 Performance assessment of CO_2 methanation on Ni/$Ca_xCe_{1-x}O_y$ catalysts involves (a) CO_2 conversion, (b) CH_4 selectivity, and (c) Arrhenius plots for CO_2 methanation. (d) The intrinsic activity and the dispersion of the catalyst. The activity tests reveal a lattice capacity threshold effect, with the maximum solid-solution pure-phase sample being at the CeO_2 lattice capacity threshold. This results in the generation of more high-activity oxygen vacancies, leading to its optimal catalytic performance (see Fig. 3, 5, 6 and Table 2).

Table 2 The reactivity of the catalysts

Catalysts	S_{BET}[a]	Dispersion[b] (%)	R_w[c] (10^{-3} mmol s^{-1} g^{-1})	R_s[c] (10^{-3} mmol s^{-1} m^{-2})	TOF[d] (s^{-1})	E_a [kJ mol^{-1}]
Ni/CeO_2	21	2.22	1.97	0.94	0.035	122.4
$Ni/Ca_{0.05}Ce_{0.95}O_y$	17	3.12	3.36	1.97	0.054	113.1
$Ni/Ca_{0.1}Ce_{0.9}O_y$	18	3.77	10.91	6.06	0.100	88.7
$Ni/Ca_{0.125}Ce_{0.875}O_y$	16	3.54	6.92	4.32	0.088	94.5
$Ni/Ca_{0.25}Ce_{0.75}O_y$	16	3.36	2.54	1.59	0.042	119.7
$Ni/Ca_{0.4}Ce_{0.6}O_y$	15	2.46	1.62	1.08	0.040	124.1

[a] Measured by BET results. [b] The absolute dispersion measured by H_2-TPD results. [c] R_w and R_s were differential rates at 250 °C, standardized based on the catalyst's weight and surface area, respectively. [d] Calculated based on the steady state CO_2 conversion at 250 °C.

mined the apparent activation energies (Table 2) for the catalysts using the formulas derived from the Arrhenius plots. In the case of the two samples containing a pure CeO_2 solid solution phase, $Ni/Ca_{0.05}Ce_{0.95}O_y$ and $Ni/Ca_{0.1}Ce_{0.9}O_y$, both the R_w and R_s values show an increasing trend as the calcium oxide doping content rises. However, in contrast, among the $Ni/Ca_{0.25}Ce_{0.75}O_y$ and $Ni/Ca_{0.4}Ce_{0.6}O_y$ catalysts, these three heterogeneous solid solution samples exhibited the presence of $CaCO_3$ on the surface of the $Ca_xCe_{1-x}O_y$ support. In this case, both the R_w and R_s values showed a significant downward trend (Fig. 3d and Table 2). The observed activity sequence, which reflected the catalytic performance of $Ni/Ca_xCe_{1-x}O_y$, appeared to be closely linked to the location of calcium within/on the CeO_2 lattice. It was noteworthy that both the R_w and R_s values followed the sequence $Ni/Ca_{0.1}Ce_{0.9}O_y$ > $Ni/Ca_{0.125}Ce_{0.875}O_y$ > $Ni/Ca_{0.05}Ce_{0.95}O_y$ > $Ni/Ca_{0.25}Ce_{0.75}O_y$ > $Ni/Ca_{0.4}Ce_{0.6}O_y$ ≫ Ni/CeO_2. These analysis results, illustrating the incorporation of Ca^{2+} into the CeO_2 lattice and forming pure solid solution structure, have potential to enhance the activity compared to heterogeneous solid solution samples accompanied by $CaCO_3$ on the $Ca_xCe_{1-x}O_y$ support surface. Additionally, the activation energy results also provided additional evidence that the incorporation of CaO into the CeO_2 lattice can reduce the activation energy in the case of pure solid solution samples. Next, the turnover frequencies (TOF) for CO_2 conversion on the exposed surface Ni active sites were calculated at 250 °C (Table 2). It is noteworthy that all the solid solution $Ni/Ca_xCe_{1-x}O_y$ catalysts exhibited significantly higher TOF values (ranging from 0.040 to 0.100 s^{-1}) compared to the unmodified Ni/CeO_2 catalyst (0.035 s^{-1}).

In a briefly general summary, solid solution samples $Ni/Ca_xCe_{1-x}O_y$ exhibited a notable enhancement in their intrinsic activity. The enhanced activity indicated the presence of a lattice capacity threshold effect in the reactivity of solid solution oxides.

The pattern of presentation was closely linked to the location of Ca (*i.e.*, in/on the support) and pure solid solutions generated the highest oxygen vacancy concentration. Hence, a pure solid solution crystal phase (*i.e.*, calcium ions incorporated into the crystalline lattice structure of CeO_2) and proper condense of moderate alkalinity are key factors to promote low-temperature activity.

The optimal sample's catalytic performance was subjected to a 20-hour stability test at 290 °C, during which no decline in the catalytic stability was observed. The stability plot is depicted below, with the corresponding text and descriptions highlighted in red font within the main text. The alkaline earth metal Ca modified the CeO_2 support, generating active oxygen vacancies. This facilitated CO_2 activation, leading to improved catalyst stability (Fig. S5†).

3.3 Studying interactions on metal and supports through H_2-TPR

To gain insight into the redox behaviors of $Ca_xCe_{1-x}O_y$ solid solution supports and the metal–support interaction, H_2-TPR experiments were performed on $Ca_xCe_{1-x}O_y$ and $NiO/Ca_xCe_{1-x}O_y$ (Fig. 4 and Table S3†). The parent CeO_2 exhibited two distinct reduction peaks, one at approximately 480 °C and another at about 780 °C. These peaks are associated with the conversion of surface Ce^{4+} into Ce^{3+} and the transformation of a fraction of the bulk CeO_2 into Ce_2O_3.[45,46]

Compared to the unaltered CeO_2, all $Ca_xCe_{1-x}O_y$ supports demonstrated similar reduction peaks. However, there was a noticeable shift of the reduction peak at ~480 °C towards a lower temperature range, suggesting the increased reducibility of the surface CeO_2 species. For Ni/CeO_2, a distinctive peak emerges at approximately 336 °C when comparing with the CeO_2 support profile. This peak can be confidently ascribed to the conversion of NiO species into metallic Ni through reduction. On the contrary, the reduction peak of NiO in the profiles of the $Ni/Ca_xCe_{1-x}O_y$ catalysts shifted to higher temperatures and became broader. This phenomenon directly indicated that the incorporation of Ca cations strengthened the interplay between NiO and the $Ca_xCe_{1-x}O_y$ supports. Hence, when compared to the unmodified Ni/CeO_2 material, the reduced $Ni/Ca_xCe_{1-x}O_y$ catalysts exhibited a smaller metallic Ni and a higher Ni dispersion (Tables S2 and S3†). Additionally, the capacity threshold effect seemed to be evident in the interaction between the metal and the support material. However, the disparity in the strength of interaction between the metal and the support was not as pronounced; thus, the impact on the activity was relatively minor. The determination of H_2 consumption and the H/Ni atomic ratios of the samples were carried out after subtracting the consumption associated with the $Ca_xCe_{1-x}O_y$ supports (Table S3†). The catalysts exhibited H/Ni atomic ratios that were close to the stoichiometric value of 2. This observation substantiated that NiO

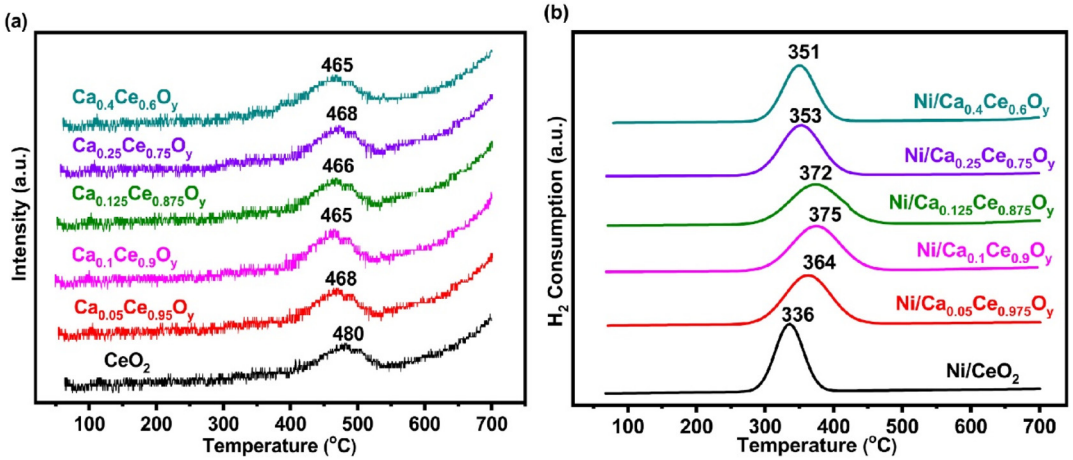

Fig. 4 H_2-TPR profiles of (a) the $Ca_xCe_{1-x}O_y$ support and (b) the fresh $Ni/Ca_xCe_{1-x}O_y$ catalysts. The capacity threshold effect appeared in the interaction between the metal and the support material. Nevertheless, the difference in the strength of this interaction was not very pronounced, resulting in a relatively minor impact on the activity (see Fig. 4 and Table S3†).

was the prevailing component in all of the samples and underwent complete reduction after hydrogen reduction pretreatment.

3.4 Oxygen properties of supports and catalysts analyzed by Raman and EPR spectroscopy

Raman characterization was employed to study the effects of Ca modification on the structure and surface oxygen vacancies. For the Raman spectrum of $Ca_xCe_{1-x}O_y$ supports (Fig. 5a–c), three distinct peaks were observed at 460, 570, and 1068 cm^{-1}, corresponding to octahedrally symmetrical vibration modes (F_{2g}), vacancy-induced modes, and superoxide (O_2^-) modes,[47] respectively. Although all samples exhibited the same signal, there was a significant variation in intensity. The ratio of the peak intensities at 570 nm and 460 nm, referred to as I_{570}/I_{460}, is commonly used as an indicative measure of the concentration of oxygen vacancies in CeO_2-based materials. The I_{570}/I_{460} values obey the order $Ca_{0.1}Ce_{0.9}O_y$ > $Ca_{0.125}Ce_{0.875}O_y$ > $Ca_{0.05}Ce_{0.95}O_y$ > $Ca_{0.25}Ce_{0.75}O_y$ > $Ca_{0.4}Ce_{0.6}O_y$ > CeO_2, where $Ca_{0.1}Ce_{0.9}O_y$ displayed the most pronounced concentration of surface oxygen vacancies. This indicated that the density of oxygen vacancies in the solid solution also exhibited a lattice capacity threshold effect. Additionally, to semi-quantify the amount of O_2^-, we calculated the I_{1068}/I_{460} values for $Ca_xCe_{1-x}O_y$ (Table S4†). Interestingly, the order of the I_{1068}/I_{460} values mirrors that of the I_{570}/I_{460} values, illustrating that O_2^- species were primarily generated through the adsorption of oxygen at these oxygen vacancies.[48] Furthermore, the modification involving Ca^{2+} cations induced the formation of a greater number of O_2^- species compared to unmodified CeO_2. Thus, when comparing the Ca-modified supports to the parent CeO_2, the former exhibited a broader F_{2g} Raman signal, indicating that Ca^{2+} ions were likely incorporated into the CeO_2

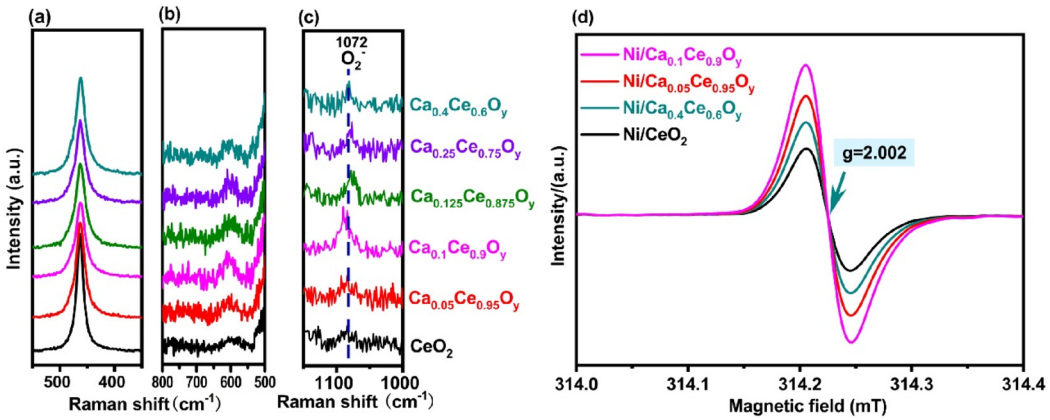

Fig. 5 Raman spectra of the $Ca_xCe_{1-x}O_y$ supports. (a) Octahedrally symmetrical vibration modes (F_{2g}); (b) vacancy-induced modes; (c) superoxide (O_2^-) modes and (d) EPR spectra of some typical $Ni/Ca_xCe_{1-x}O_y$ catalysts. The results reveal a lattice capacity threshold effect, with the maximum solid-solution pure-phase sample being at the CeO_2 lattice capacity threshold (see Fig. 5, 6, 8 and Table S4†).

lattice matrix, which in turn affects the crystallinity (Fig. 5a). Interestingly, it is noteworthy that $Ca_{0.1}Ce_{0.9}O_y$ exhibited the highest concentration of O_2^- species among all the $Ca_xCe_{1-x}O_y$ supports. Raman spectroscopy results confirmed that introducing different levels of Ca^{2+} cations elevated both the density of oxygen vacancies and the quantity of O_2^- species, exhibiting a lattice capacity threshold effect. The modification of the solid solution supports has a notable impact on the surface characteristics of $Ni/Ca_xCe_{1-x}O_y$, which will be investigated further in conjunction with XPS and CO_2-TPD analysis.

EPR spectroscopy was employed to further characterize the O_2^- species with electromagnetism on the catalyst surface for some typical reduced catalysts (Fig. 5d). Notably, distinct EPR signals corresponding to O_2^- emerged, specifically with a g value of 2.002. The intensity of the O_2^- signal peaks followed the sequence $Ni/Ca_{0.1}Ce_{0.9}O_y$ > $Ni/Ca_{0.05}Ce_{0.95}O_y$ > $Ni/Ca_{0.4}Ce_{0.6}O_y$ > Ni/CeO_2, where $Ni/Ca_{0.1}Ce_{0.9}O_y$ showcased the most pronounced accumulation of surface oxygen vacancies, aligning with the Raman spectroscopy results. In summary, both EPR and Raman results consistently demonstrated a lattice capacity threshold effect for oxygen vacancies in both the support and supported Ni-based catalysts.

3.5 Exploring the lattice capacity threshold effect of oxygen vacancies and moderate alkali center contents *via* XPS and CO_2-TPD

The surface elements of the reduced catalysts were assessed through XPS. The Ce 3d spectra were deconvoluted and analyzed (Fig. 6a and Table S5†). Each spectrum was deconvoluted into 10 groups corresponding to the surface species of Ce^{3+} and Ce^{4+}, with the full width at half maximum (FWHM) of a single Ce peak fixed in the range of 2.9–3.3 eV.[49] The six characteristic peaks at u‴ (916.1 eV), u″ (907.2 eV), u′ (900.7 eV), v‴ (898.0 eV), v″ (888.6 eV) and v (882.2 eV) were assigned to the Ce^{4+} species. In contrast, the remaining four peaks at u′ (903.9 eV), u_0 (899.3 eV), v′ (884.4 eV), and v_0 (880.6 eV) were attributed to Ce^{3+} species. To conduct an investigation into the promotional effect of calcium on the surface Ce^{3+} concentration, the surface $Ce^{3+}/(Ce^{3+} + Ce^{4+})$ ratios were determined by dividing the ratio of the integrated areas of the Ce^{3+} peaks with the sum of the integrated areas of both the Ce^{3+} and Ce^{4+} peaks.[50] Previous works have indicated a strong correlation between the quantity of oxygen vacancies on the surface of CeO_2 and the concentration of Ce^{3+} ions on the surface.[51,52] The observed surface ratios of $Ce^{3+}/(Ce^{3+} + Ce^{4+})$ followed the

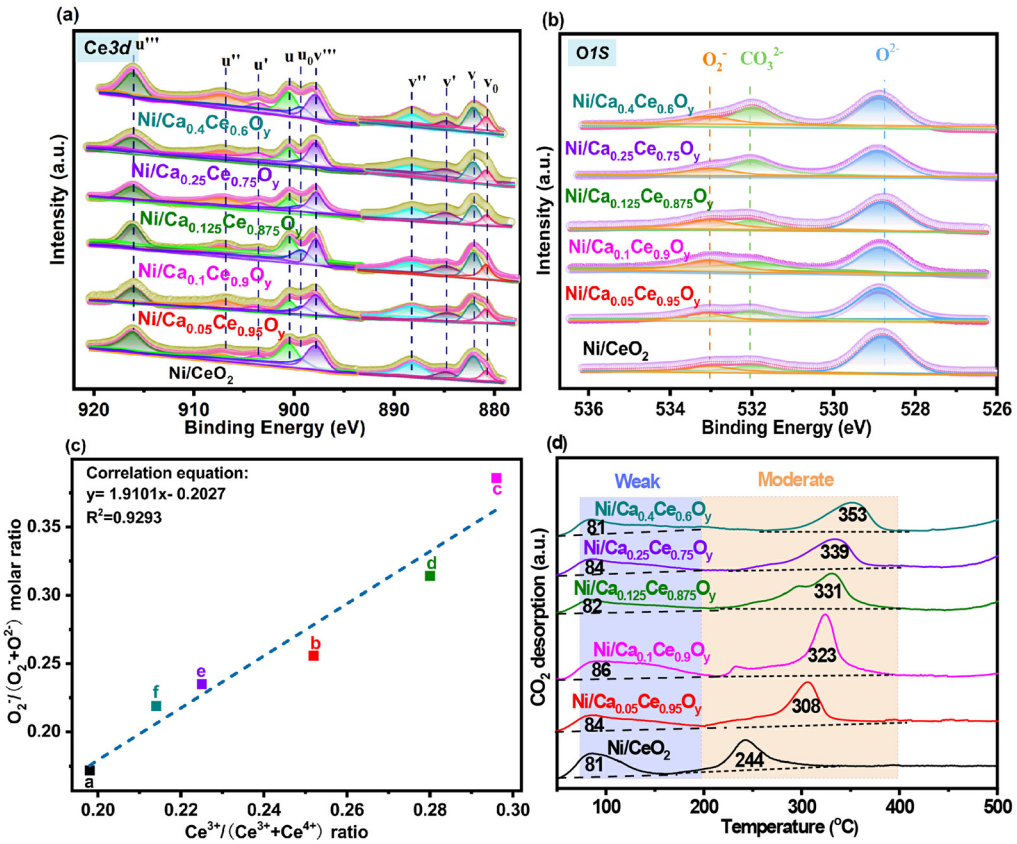

Fig. 6 XPS spectra of $Ni/Ca_xCe_{1-x}O_y$ catalysts (a) Ce 3d; (b) O 1s; (c) the correlation of surface $O_2^-/(O_2^- + O^{2-})$ ratio *versus* $Ce^{3+}/(Ce^{3+} + Ce^{4+})$ ratios; (d) CO_2 desorption profiles of the $Ni/Ca_xCe_{1-x}O_y$ catalysts. (a. Ni/CeO_2; b. $Ni/Ca_{0.05}Ce_{0.95}O_y$; c. $Ni/Ca_{0.1}Ce_{0.9}O_y$; d. $Ni/Ca_{0.125}Ce_{0.875}O_y$; e. $Ni/Ca_{0.25}Ce_{0.75}O_y$; f. $Ni/Ca_{0.4}Ce_{0.6}O_y$). The lattice capacity threshold effect in the presence of oxygen vacancies and moderate-strength alkali centers was primarily attributed to the lattice capacity threshold effect (see Fig. 5, 6 and Table S5†).

particular sequence of $Ni/Ca_{0.1}Ce_{0.9}O_y$ > $Ni/Ca_{0.125}Ce_{0.875}O_y$ > $Ni/Ca_{0.05}Ce_{0.95}O_y$ > $Ni/Ca_{0.25}Ce_{0.75}O_y$ > $Ni/Ca_{0.4}Ce_{0.6}O_y$ > Ni/CeO_2. These results aligned well with the density of oxygen vacancies on the surface of $Ca_xCe_{1-x}O_y$, as determined through Raman spectroscopy (Tables S4 and S5†). This further validated the presence of an oxygen vacancy lattice capacity threshold effect in the sample with the best catalytic performance. The surface Ca/(Ce + Ca) ratios of $Ni/Ca_{0.05}Ce_{0.95}O_y$ and $Ni/Ca_{0.1}Ce_{0.9}O_y$ catalysts were found to be slightly elevated compared to their stoichiometric ratios in the bulk material. This observation suggested that a substantial portion of the Ca^{2+} cations was effectively incorporated into the CeO_2 lattice, resulting in the formation of a solid solution structure. Conversely, the surface Ca/(Ce + Ca) ratios in the $Ni/Ca_{0.125}Ce_{0.875}O_y$, $Ni/Ca_{0.25}Ce_{0.75}O_y$, and $Ni/Ca_{0.4}Ce_{0.6}O_y$ catalysts were significantly elevated compared to their stoichiometric ratios in the $Ca_xCe_{1-x}O_y$ bulk materials, indicating that Ca^{2+} cations were mainly found as scattered carbonate deposits on the support surfaces. Higher surface oxygen vacancies were expected to lead to more active oxygen species on the catalysts' surface due to the increased adsorption of gas-phase O_2 molecules. We deconvoluted and analyzed the O 1s spectra for the reduced catalysts (Fig. 6b). Three distinct peaks representing O_2^- (533.0–533.1 eV), CO_3^{2-} (531.9–532.2 eV), and the lattice oxygen O^{2-} (528.6–529.2 eV) were identified based on a single oxygen peak with an FWHM of 1.8–2.0 eV.[53] $O_2^-/(O_2^- + O^{2-})$; the ratio between the surface O_2^- and lattice oxygen amount was quantified (Table S5†). The intimate correlation of surface $O_2^-/(O_2^- + O^{2-})$ ratios with the $Ce^{3+}/(Ce^{3+} + Ce^{4+})$ ratios (Fig. 6c) showcased that surface-bound O_2^- originates from O_2 adsorption at the oxygen vacancies.

CO_2 adsorption/desorption technique was employed to assess the surface alkalinity of the reduced catalysts (Fig. 6d and Table S5†). Several distinct CO_2 desorption peaks were observed at temperatures below 450 °C. Peaks occurring at temperatures below 200 °C and between 200 and 450 °C were identified as weak and moderate alkaline sites, respectively. Here, the weak alkaline sites were reported as surface OH groups, followed by oxygen vacancies as moderate alkaline sites.[51] The combined quantity of alkaline sites and the quantity of moderate alkaline sites followed the sequence $Ni/Ca_{0.1}Ce_{0.9}O_y$ > $Ni/Ca_{0.125}Ce_{0.875}O_y$ > $Ni/Ca_{0.05}Ce_{0.95}O_y$ > $Ni/Ca_{0.25}Ce_{0.75}O_y$ > $Ni/Ca_{0.4}Ce_{0.6}O_y$ > Ni/CeO_2 (Table S5†). This trend aligned with the intrinsic activity (R_s) sequence (Tables 2 and S5†), which reaffirmed the lattice capacity threshold effect on the concentration of medium-strength alkali centers generated by oxygen vacancies in solid solutions. $Ni/Ca_{0.1}Ce_{0.9}O_y$ and $Ni/Ca_{0.125}Ce_{0.875}O_y$, the two highly active catalysts, not only exhibited a significantly higher quantity of moderate alkaline sites but also demonstrated elevated CO_2 desorption temperatures compared to the other samples, indicating that both weak and moderate alkaline sites facilitated the CO_2 methanation reaction, with the moderate alkaline sites playing a primary role in determining the activity.

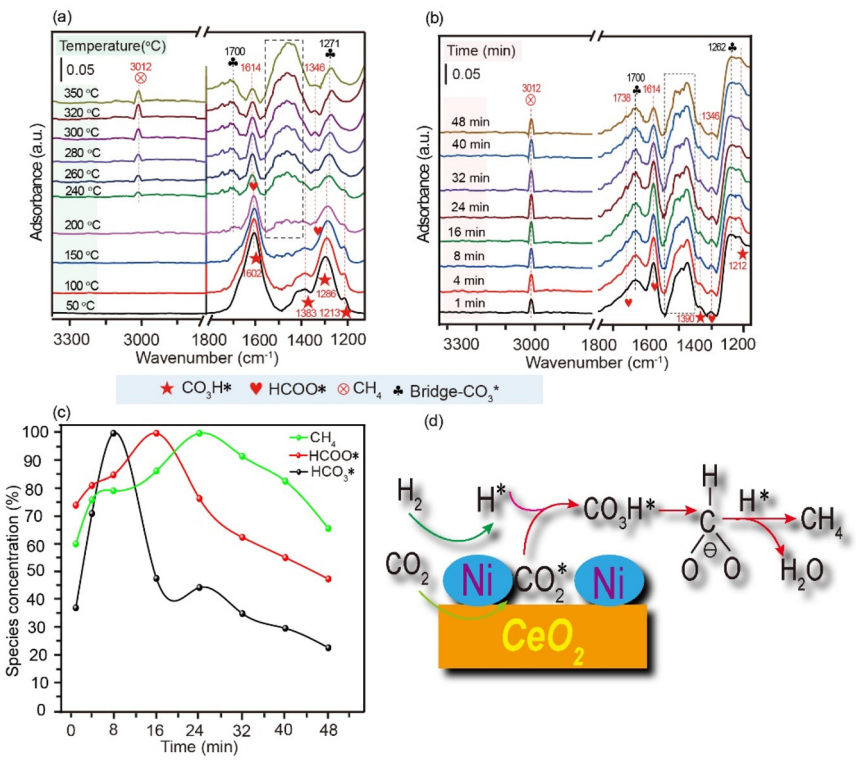

Fig. 7 *In situ* FTIR spectra on the Ni/CeO_2 catalyst, (a) tendency over temperature; (b) tendency over time; (c) dynamic evolution of reaction intermediates chart; (d) proposed possible reaction mechanism ($CO_3H^* \rightarrow HCOO^* \rightarrow CH_4$).

3.6 *In situ* FTIR investigation of the reaction path of Ni/CeO_2 for CO_2 methanation

In situ FTIR experiments were conducted to detect the reaction intermediates during CO_2 hydrogenation on the Ni/CeO_2 catalyst. The signals (1213, 1286, 1383 cm^{-1}, and 1602 cm^{-1}) were attributed to bicarbonate (CO_3H^*) species[54–56] at 50 °C (Fig. 7a). As the temperature increased, the intensity of these CO_3H^* species gradually decreased and nearly disappeared at 260 °C. The peaks at 1271 and 1700 cm^{-1} were associated with bridged carbonate,[57] while peaks in the range of 1550–1350 cm^{-1} correspond to carbonate species.[58] As the CO_3H^* species were consumed, formates (HCOO*) began to emerge (1346 and 1614 cm^{-1}).[54,56,59] The intensity of HCOO* significantly increased between 200 °C and 280 °C and then declined. Notably, a new peak at 3012 cm^{-1} emerged, which was attributed to the CH_4^* species under 240 °C. These results suggested that CH_4 formation may originate from HCOO* species during CO_2 methanation on the Ni/CeO_2 catalyst.

To better illustrate the mutual conversion among intermediate species and their relationships (CO_3H^*, HCOO*, CH_4^*), *in situ* infrared testing was conducted at 240 °C (Fig. 7b). Prior to conducting the experiment on the temporal dynamics of the intermediate species, the catalyst underwent a pre-treatment at 300 °C in a high-purity Ar atmosphere for 1 h to eliminate surface impurities. Following this, the temperature was reduced to room temperature. After background subtraction, a mixed gas containing 1% CO_2, 4% H_2, and 95% Ar was introduced. Subsequently, rapid heating from ambient temperature to 240 °C was carried out to investigate the dynamic variations among the intermediate species at this temperature. The formation of formate (HCOO*) initially increased, reaching its maximum at 16 min, while methane (CH_4^*) also exhibited an initial increase tendency, reaching its maximum at 24 min (Fig. 7b).

To illustrate the dynamic changes in the intermediate species and the methane formation mechanism, we plotted the integrated peak areas of all the carbonate, formate, and methane species, setting the peak area with the highest value to 100%. This allowed us to observe the percentage content trends of these three species (Fig. 7c). It was evident that CO_3H^* initially increased, reached a maximum at 8 min, and then gradually decreased, stabilizing after 40 min. Concurrently, as CO_3H^* was rapidly consumed, HCOO* exhibited a similar trend, increasing until 16 min and then stabilizing after 40 min. As HCOO* was consumed, the CH_4 content

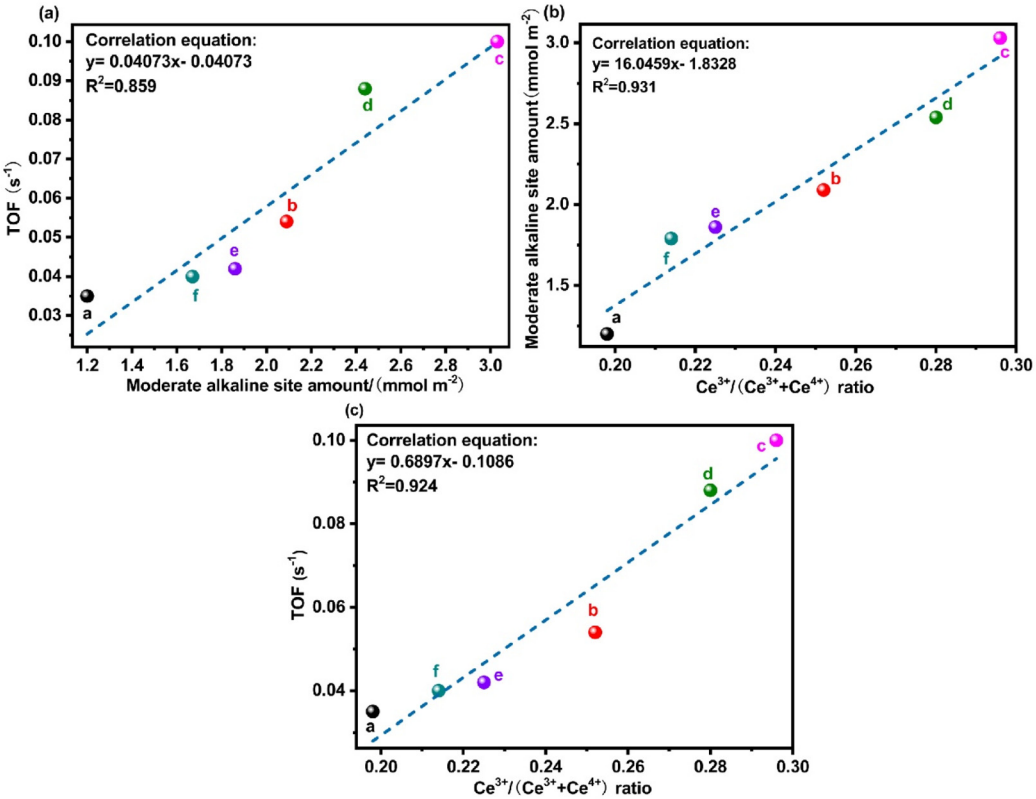

Fig. 8 (a) Correlation between the TOF values at 250 °C and the amount of surface moderate alkaline sites, (b) the correlation between the surface moderate alkaline sites and $Ce^{3+}/(Ce^{3+} + Ce^{4+})$ ratio, and (c) the correlation between the TOF values at 250 °C and $Ce^{3+}/(Ce^{3+} + Ce^{4+})$ ratios. (a. Ni/CeO_2; b. $Ni/Ca_{0.05}Ce_{0.95}O_y$; c. $Ni/Ca_{0.1}Ce_{0.9}O_y$; d. $Ni/Ca_{0.125}Ce_{0.875}O_y$; e. $Ni/Ca_{0.25}Ce_{0.75}O_y$; f. $Ni/Ca_{0.4}Ce_{0.6}O_y$). The lattice capacity threshold effect in the presence of oxygen vacancies and moderate-strength alkali centers was primarily attributed to the lattice capacity threshold effect.

followed a pattern of initial increase, reaching its maximum at 24 min. Throughout this process, CO_3H^*, HCOO*, and CH_4 coexisted, indicating a dynamic equilibrium in their conversion.

Based on the aforementioned findings, a CO_2 methanation mechanism was proposed. CO_2 interacted with the surface OH sites, forming CO_3H^* at low temperatures. As the temperature increased, CO_3H^* was transformed into HCOO*, which subsequently evolved into CH_4* (Fig. 7d).

3.7 The network of structure–activity relationship

It should be noted that surface oxygen vacancies play a pivotal role as highly active alkaline sites for CO_2 adsorption and conversion.[11,60] These sites, stemming from surface oxygen vacancies, serve as affordably reactive moderate alkaline sites on CeO_2-based catalysts for various CO_2 conversion reactions.[11,51,61,62] Hence, to better understand the relationship between oxygen vacancies, intermediate alkali centers, and turnover frequency (TOF), the relevant correlation lines were plotted. The linear correlation between surface oxygen vacancies and moderate alkaline sites further proved that the moderate alkaline sites were primarily assigned to the surface oxygen vacancies of Ni/$Ca_xCe_{1-x}O_y$ catalysts (Fig. 8a). A clear and direct linear relationship was evident between the TOF values and the abundance of moderate alkaline sites (Fig. 8b). Catalysts with a higher concentration of moderate alkaline sites exhibited superior intrinsic activity for CO_2 methanation, underscoring the pivotal role of these sites in the catalytic performance. Notably, surface oxygen vacancies, serving as alkaline sites, are expected to enhance CO_2 activation. Evidently, there was a linear correlation between intrinsic catalytic performance and the amount of surface oxygen vacancies (Fig. 8c). Catalysts with a higher concentration of surface oxygen vacancies exhibited favorable intrinsic activity for CO_2 methanation.

In summary, oxygen vacancies in solid solutions can serve as highly active catalytic sites at the reaction interface during the CO_2 methanation reaction, which enhances CO_2 adsorption activation and significantly boosts low-temperature reactivity. The presence of moderately strong alkaline centers in solid solution materials originated from oxygen defect sites, and the content of these alkaline centers determined the reaction activity. Here, Ni/$Ca_{0.1}Ce_{0.9}O_y$, due to the presence of the maximum amount of the pure solid solution phase, generates the highest number of oxygen vacancies. The lattice capacity effect resulting from the oxygen vacancies in this sample was the primary reason for the threshold effect observed in the methane conversion reactivity.

4 Conclusion

A series of Ni/$Ca_xCe_{1-x}O_y$ catalysts were synthesized through the sol–gel method and employed for CO_2 methanation to investigate the impact of Ca^{2+} incorporation into the CeO_2 lattice on the structure–activity relationship of supported Ni catalysts, specifically focusing on the lattice capacity threshold effect. XRD analysis was initially employed to study the solid solution structure and cell parameters, leading to the first-ever determination of the lattice capacity for Ca in CeO_2 through the XRD extrapolation method. The lattice capacity of Ca^{2+} in CeO_2 was detected for the first time, corresponding to a Ca : Ce molar ratio of 11 : 89. The catalytic materials in the Ni/$Ca_xCe_{1-x}O_y$ series exhibited a lattice capacity threshold effect due to the presence of alkaline centers generated by oxygen vacancies. This lattice capacity threshold effect was the primary reason for the enhanced activity observed in these catalysts during the CO_2 methanation reaction. While the interaction between the metal and the support as well as the metal Ni exhibiting lattice capacity threshold effects promote the enhancement of the activity, they were not the primary factors contributing to the lattice capacity threshold effect in the active sites. Furthermore, the potential reaction pathway of Ni/CeO_2 catalyst in the CO_2 methanation was revealed ($CO_3H^* \rightarrow HCOO^* \rightarrow CH_4$).

This study established a distinct correlation between oxygen vacancies and intrinsic activity through XRD extrapolation. The initial exploration unveiled the presence of a lattice capacity threshold effect in composite catalysts composed of metal oxide-supported Ni, which offers crucial insights for optimizing low-temperature CO_2 methanation performance.

Conflicts of interest

The authors declare that they have no known competing financial interests or personal relationships that could have appeared to influence the work reported in this paper.

Acknowledgements

The authors are grateful for financial support from the National Natural Science Foundation of China (22062013 and 22262021), the Jiangxi Provincial Natural Science Foundation (20212BAB203030, 20232ACB213002, and 20192BAB206035), and the Key Laboratory Foundation of Jiangxi Province for Environment and Energy Catalysis (20181BCD40004).

References

1 F. Tian, X. Wu, J. Chen, X. Sun, X. Yan and G. Liao, *Dalton Trans.*, 2023, **52**, 11934–11940.
2 G. Ding, C. Li, Y. Ni, L. Chen, L. Shuai and G. Liao, *EES Catal.*, 2023, **1**, 369–391.
3 Q. Zhang, G. Liao, B. Yang, Y. Zhang, G. Ge, A. Lipovka, J. Liu, R. D. Rodriguez, X. Yang and X. Jia, *Appl. Surf. Sci.*, 2023, **638**, 157989.
4 G. Liao, C. Li, S.-Y. Liu, B. Fang and H. Yang, *Phys. Rep.*, 2022, **983**, 1–41.
5 G. Liao, Y. He, H. Wang, B. Fang, N. Tsubaki and C. Li, *Device*, 2023, **1**, 100173.

6 G. Liao, G. Ding, B. Yang and C. Li, *Precis. Chem.*, 2024, **2**, 49–56.
7 K. Wei, H. Guan, Q. Luo, J. He and S. Sun, *Nanoscale*, 2022, **14**, 11869–11891.
8 F. M. Mota and D. H. Kim, *Chem. Soc. Rev.*, 2019, **48**, 205–259.
9 S. Rönsch, J. Schneider, S. Matthischke, M. Schlüter, M. Götz, J. Lefebvre, P. Prabhakaran and S. Bajohr, *Fuel*, 2016, **166**, 276–296.
10 M. Younas, L. L. Kong, M. J. K. Bashir, H. Nadeem, A. Shehzad and S. Sethupathi, *Energy Fuels*, 2016, **30**, 8815–8831.
11 K. Liu, X. Xu, J. Xu, X. Fang, L. Liu and X. Wang, *J. CO_2 Util.*, 2020, **38**, 113–124.
12 B. Li, B. Ma, S.-Y. Wang, M.-M. Yu, Z.-Q. Zhang, M.-J. Xiao, H. Zhang, J.-F. Wu, Y. Peng, Q. Wang and H.-L. Zhang, *Nanoscale*, 2022, **14**, 9736–9742.
13 L. P. L. Gonçalves, M. Meledina, A. Meledin, D. Y. Petrovykh, J. P. S. Sousa, O. S. G. P. Soares, Y. V. Kolen'ko and M. F. R. Pereira, *Carbon*, 2022, **195**, 35–43.
14 L. Zhong, H. Zheng, C. Du, W. Du, G. Liao, C. S. Cheung and H. Gao, *J. Catal.*, 2020, **384**, 208–217.
15 C. Italiano, J. Llorca, L. Pino, M. Ferraro, V. Antonucci and A. Vita, *Appl. Catal., B*, 2020, **264**, 118494.
16 X. Jia, X. Zhang, N. Rui, X. Hu and C.-J. Liu, *Appl. Catal., B*, 2019, **244**, 159–169.
17 J. K. Prabhakar, P. A. Apte and G. Deo, *Chem. Eng. J.*, 2023, **471**, 144252.
18 R.-P. Ye, Q. Li, W. Gong, T. Wang, J. J. Razink, L. Lin, Y.-Y. Qin, Z. Zhou, H. Adidharma, J. Tang, A. G. Russell, M. Fan and Y.-G. Yao, *Appl. Catal., B*, 2020, **268**, 118474.
19 C. Li, B. Cheng, H. Lu, G. Ding, Z. Jiang and G. Liao, *Inorg. Chem.*, 2023, **62**, 6843–6850.
20 G. Liao, Z. Xiao, X. Chen, C. Du, L. Zhong, C. S. Cheung and H. Gao, *Macromolecules*, 2020, **53**, 256–266.
21 S. Tada, T. Shimizu, H. Kameyama, T. Haneda and R. Kikuchi, *Int. J. Hydrogen Energy*, 2012, **37**, 5527–5531.
22 G. Liao, L. Zhang, C. Li, S.-Y. Liu, B. Fang and H. Yang, *Matter*, 2022, **5**, 3341–3374.
23 B. Nematollah, M. Rezaei and E. N. Lay, *J. Rare Earths*, 2015, **33**, 619–628.
24 R. Daroughegi, F. Mwshkani and M. Rezaei, *Chem. Eng. Sci.*, 2020, **2302**, 41–50.
25 Z. Zhang, Y. Tong, X. Fang, J. Xu, X. Xu and X. Wang, *Fuel*, 2022, **316**, 123191.
26 N. Rui, X. Zhang, F. Zhang, Z. Liu, X. Cao, Z. Xie, R. Zou, S. D. Senanayake, Y. Yang, J. A. Rodriguez and C.-J. Liu, *Appl. Catal., B*, 2021, **282**, 119581.
27 S. Lin, Z. Hao, J. Shen, X. Chang, S. Huang, M. Li and X. Ma, *J. Energy Chem.*, 2021, **59**, 334–342.
28 L. Lin, C. A. Gerlak, C. Liu, J. Llorca, S. Yao, N. Rui, F. Zhang, Z. Liu, S. Zhang, K. Deng, C. B. Murray, J. A. Rodriguez and S. D. Senanayake, *J. Energy Chem.*, 2021, **61**, 602–611.
29 Y. Xie, J. Chen, X. Wu, J. Wen, R. Zhao, Z. Li, G. Tian, Q. Zhang, P. Ning and J. Hao, *ACS Catal.*, 2022, **12**, 10587–10602.
30 G. Liao, J. Fang, Q. Li, S. Li, Z. Xu and B. Fang, *Nanoscale*, 2019, **11**, 7062–7096.
31 X. Xu, L. Liu, Y. Tong, X. Fang, J. Xu, D.-E. Jiang and X. Wang, *ACS Catal.*, 2021, **11**, 5762–5775.
32 W.-T. Chen, K.-B. Chen, M.-F. Wang, S.-F. Weng, C.-S. Lee and M. C. Lin, *Chem. Commun.*, 2010, **46**, 3286–3288.
33 J. Sun, Y. Lu, L. Zhang, C. Ge, C. Tang, H. Wan and L. Dong, *Ind. Eng. Chem. Res.*, 2017, **56**, 12101–12110.
34 J. Y. Wei, Y. X. Zhu, L. Y. Duan and Y. C. Xie, *Chin. J. Catal.*, 2003, **24**, 414–418.
35 X. Yao, C. Tang, Z. Ji, Y. Dai, Y. Cao, F. Gao, L. Dong and Y. Chen, *Catal. Sci. Technol.*, 2013, **3**, 688–698.
36 P. Zhang, H. Lu, Y. Zhou, L. Zhang, Z. Wu, S. Yang, H. Shi, Q. Zhu, Y. Chen and S. Dai, *Nat. Commun.*, 2015, **6**, 8446.
37 X. Yao, Y. Xiong, W. Zou, L. Zhang, S. Wu, X. Dong, F. Gao, Y. Deng, C. Tang, Z. Chen, L. Dong and Y. Chen, *Appl. Catal., B*, 2014, **144**, 152–165.
38 P. F. Zhang, H. F. Lu, Y. Zhou, L. Zhang, Z. L. Wu, S. Z. Yang, H. L. Shi, Q. L. Zhu, Y. F. Chen and S. Dai, *Nat. Commun.*, 2015, **6**, 10.
39 Z. Zhang, Y. Tong, X. Fang, J. Xu, X. Xu and X. Wang, *Fuel*, 2022, **316**, 123191.
40 M. Sugiura, *Catal. Surv. Asia*, 2003, **7**, 77–87.
41 Q. Sun, X. Xu, H. Peng, X. Fang, W. Liu, J. Ying, F. Yu and X. Wang, *Chin. J. Catal.*, 2016, **37**, 1293–1302.
42 X. Xu, F. Liu, X. Han, Y. Wu, W. Liu, R. Zhang, N. Zhang and X. Wang, *Catal. Sci. Technol.*, 2016, **6**, 5280–5291.
43 Y. Xie and Y. Tang, *Adv. Catal.*, 1990, **37**, 1–43.
44 X. Xu, F. Liu, J. Tian, H. Peng, W. Liu, X. Fang, N. Zhang and X. Wang, *ChemPhysChem*, 2017, **18**, 1533–1540.
45 X. Lin, S. Li, H. He, Z. Wu, J. Wu, L. Chen, D. Ye and M. Fu, *Appl. Catal., B*, 2018, **223**, 91–102.
46 J. Xu, L. Peng, X. Fang, Z. Fu, W. Liu, X. Xu, H. Peng, R. Zheng and X. Wang, *Appl. Catal., A*, 2018, **552**, 117–128.
47 J. Xu, Y. Zhang, X. Xu, X. Fang, R. Xi, Y. Liu, R. Zheng and X. Wang, *ACS Catal.*, 2019, **9**, 4030–4045.
48 Z.-Y. Pu, X.-S. Liu, A.-P. Jia, Y.-L. Xie, J.-Q. Lu and M.-F. Luo, *J. Phys. Chem. C*, 2008, **112**, 15045–15051.
49 F. Larachi, J. Pierre, A. Adnot and A. Bernis, *Appl. Surf. Sci.*, 2002, **195**, 236–250.
50 Z. Hu, X. Liu, D. Meng, Y. Guo, Y. Guo and G. Lu, *ACS Catal.*, 2016, **6**, 2265–2279.
51 F. Wang, M. Wei, D. G. Evans and X. Duan, *J. Mater. Chem. A*, 2016, **4**, 5773–5783.
52 Z. Bian, Y. M. Chan, Y. Yu and S. Kawi, *Catal. Today*, 2020, **347**, 31–38.
53 V. J. Ferreira, P. Tavares, J. L. Figueiredo and J. L. Faria, *Ind. Eng. Chem. Res.*, 2012, **51**, 10535–10541.
54 C. Binet, M. Daturi and J. C. Lavalley, *Catal. Today*, 1999, **50**, 207–225.
55 Q. Pan, J. Peng, T. Sun, S. Wang and S. Wang, *Catal. Commun.*, 2014, **45**, 74–78.

56 Q. Pan, J. Peng, S. Wang and S. Wang, *Catal. Sci. Technol.*, 2014, **4**, 502–509.
57 C. Li, Y. Sakata, T. Arai, K. Domen, K.-I. Maruya and T. Onishi, *J. Chem. Soc., Faraday Trans. 1*, 1989, **85**, 929–943.
58 G. Marban, I. Lopez and T. Valdes-Solis, *Appl. Catal., A*, 2009, **361**, 160–169.
59 S. Haq, J. G. Love, H. E. Sanders and D. A. King, *Surf. Sci.*, 1995, **325**, 230–242.
60 B. Yang, X. Li, Q. Zhang, X. Yang, J. Wan, G. Liao, J. Zhao, R. Wang, J. Liu, R. D. Rodriguez and X. Jia, *Appl. Catal., B*, 2022, **314**, 121521.
61 J. Graciani, K. Mudiyanselage, F. Xu, A. E. Baber, J. Evans, S. D. Senanayake, D. J. Stacchiola, P. Liu, J. Hrbek, J. F. Sanz and J. A. Rodriguez, *Science*, 2014, **345**, 546–550.
62 F. Wang, S. He, H. Chen, B. Wang, L. Zheng, M. Wei, D. G. Evans and X. Duan, *J. Am. Chem. Soc.*, 2016, **138**, 6298–6305.